Detailed flow development and indicators of transition in a natural convection flow in a vertical channel

Martin Thebault, Stéphanie Giroux-Julien, Victoria Timchenko, Christophe Ménézo, John Reizes

Highlights

Detailed flow development and indicators of transition in a natural convection flow in a vertical channel.

Martin Thebault, Stéphanie Giroux–Julien, Victoria Timchenko, Christophe Ménézo, John Reizes

- Transitional natural convection is studied experimentally and numerically
- Different transition indicators are defined based on velocity and thermal quantities
- Detailed experimental and numerical mapping of the flow spatial development is provided
- Realistic environmental conditions are considered

Detailed flow development and indicators of transition in a natural convection flow in a vertical channel.

Martin Thebault[a,b], Stéphanie Giroux–Julien[a], Victoria Timchenko[b], Christophe Ménézo[c], John Reizes[b]

[a] *Univ Lyon, CNRS, INSA-Lyon, Université Claude Bernard Lyon 1, CETHIL UMR5008, F-69621, Villeurbanne, France*
[b] *School of Mechanical and Manufacturing Engineering, UNSW-Sydney, Sydney 2052, Australia*
[c] *University Savoie Mont-Blanc, LOCIE UMR CNRS 5271, Campus Scientifique Savoie Technolac – F-73376, Le Bourget-du-Lac, France*

Abstract

A spatially developing transitional flow in a vertical channel with one side heated uniformly and subjected to random velocity fluctuations at the inlet is investigated in this experimental and numerical study. Two Rayleigh numbers are studied. Experimentally, Particle Image Velocimetry is used to obtain a complete two-dimensional velocity field of the streamwise flow development. A three-dimensional Large-Eddy-Simulation investigation is also performed to obtain a complete streamwise evolution of the flow. The results allow the definition of three transition indicators on the basis of the time-averaged velocities and temperatures fields as well as on the turbulent statistics of the flow. The detailed experimental and numerical spatial development of the transitional natural convective flow is then presented and the ability of the indicators to capture the early and the advanced stages of the transition is assessed. The numerical simulations were performed on the assumptions of a thermally stratified environment, submitted to an environmental noise, and for which wall to wall radiations were considered. These conditions aim at representing realistic experimental conditions.

Keywords:
transitional natural convection, transition indicators, experimental, numerical, chimney effect

Email address: martin.thebault@univ-smb.fr (Martin Thebault)

1. Introduction

Over the last decade and a half, increasing concerns regarding the environmental issues due to anthropic global warming has spurred a rethinking of the management and methods of energy production and consumption. Since the daily incident solar energy on the global landmass is greater than the annual worldwide energy consumption, the harvesting of solar energy is one of the more promising solutions. As a result, among other technologies, passively ventilated PhotoVoltaic (PV) arrays integrated in buildings (BIPV) have been developed. These components use solar energy to generate electricity, whilst the concomitant, but unwanted thermal heating of the arrays produces natural convective flows in the space between the PV facade and the wall enclosing the building. This natural ventilation cools the PV arrays, thereby increasing their efficiency [1], with the added advantage that the flow can also be used for the heating of the building during the day or for cooling it at night.

The study of such system is challenging for several reasons. When BIPV systems operate in real-conditions, the flow is expected to be transitional or turbulent. Moreover, it is impacted by the environment, which significantly increases the complexity of the problem. Therefore, laboratory-scale experiments and numerical models often take the aspect of a heated vertical channel which represents a simplification of the problem. Natural convective flows observed in experimental channels and in numerical simulations of channels of finite sizes often display the following characteristics:

1. The flow is spatially developing over a large region;
2. Experimentally the flow is submitted to various external factors such as external thermal stratification or ambient velocity disturbances. As results, in numerical models, the boundary conditions have not yet been properly established;
3. The flow undergoes a transition from a laminar to a turbulent regime.

It therefore appears that the knowledge of these processes is inherent to the knowledge of the spatial development of the transitional flow as well as on its interaction with the environment.

Miyamoto et al. [2] performed one of the first experimental investigation dealing with transitional laminar-turbulent natural convective flows in an

isoflux vertical channel. The channel was 5 m high and a parametric study was conducted with the channel width and the heat input varied. Discrete velocity profiles, measured at different height, provided some insights of the spatial development of the flow and temperature at the walls were recorded. In each case, they observed a local maximum in the heated wall temperature which they associated with transition to turbulent flow. The same phenomenon was observed later in other experimental works [3, 4, 5, 6, 7, 8]. In a water channel uniformly heated on both sides, Daverat et al. [9] used the height at which the maximum of the velocity difference between the near wall velocity and the bulk velocity was reached as a marker of the transition. However, even if the experimental spatial resolution tends to increase, it often remains too sparse and consequently difficult to study the flow development in details in the transition region.

Since experimental techniques are sometimes limited, simulations have therefore been performed to better understand the transition phenomena which occur in this type of flow. Fedorov and Viskanta [10], using a steady-state Reynolds Averaged Navier-Stokes (RANS) solver managed to obtain qualitative agreement with the experimental results of Miyamoto et al. [2] on the location at which the temperature reaches a maximum on the heated wall, but it required very large values of turbulence levels at the inlet of the channel. More recently, Lau et al. [11] and Li et al. [12], by respectively using Large Eddy Simulation (LES) model with the Vreman Subgrid-Scale (SGS) model and Direct Numerical Simulation methodologies, obtained good agreement with the experimental results of Miyamoto et al. [2] and more particularly with the location at which the temperature reaches a maximum on the heated wall. However none of these studies analyzed in details the flow development in the transition region.

A LES study of Kogawa et al. [13] of a symmetrically heated channel, at uniform temperature associated the beginning of transition to the appearance of the Tollmien-Schlichting (TS) waves which are characteristics of the beginning of the natural transition of weakly disturbed natural convection flow [14], [15]. However, as was demonstrated by Fedorov and Viskanta [10] in a study using RANS models and by Lau et al. [16] and Tkachenko et al. [17] in LES investigations, the turbulent intensity level at the entrance of the channel proved crucial to obtaining a fairly good representation of the mean and turbulent quantities of the flow. Because of the presence of the inlet disturbances, the TS waves observed by Kogawa et al. [13] are replaced by much more complex three-dimensional structures [7, 18, 19] which make

their criteria impossible to use to locate the beginning of the transition.

It appears that, despite some improvements in the numerical/experimental agreement, the detailed experimental and numerical velocity and thermal fields have never been used concomitantly to define relevant transition indicators and to investigate in details the flow changes around them. Furthermore it appears that the transition region is not clearly defined. Indeed, despite the fact that some indicators have already been defined, transition occurs in different stages. It is therefore even less clear which stage of transition, beginning, early or advanced these indicators specify.

The literature concerning the definition of transition indicators is more exhaustive for the case of single vertical plate natural convection flow. Despite natural convection flow in vertical channel is different to those in vertical plate configuration, they are both purely buoyancy driven flow and it is expected that they share some similar mechanisms.

In an experimental study, Godaux and Gebhart [20] defined the beginning of the thermal transition as the height at which the time-averaged temperature profiles of the flow changed from the laminar ones. Jaluria and Gebhart [21] considered the beginning of the velocity transition at the height at which they could observe the first burst and instabilities. In their experimental study Mahajan and Gebhart [22] noted that this criteria could sometimes be difficult to use with noisy experimental measures and more especially in gases. For that reason they defined the beginning of the transition as *"... a decrease in the rate of increase of both the maximum velocity and the overall temperature difference, respectively from the laminar downstream trends."*, the overall temperature difference being the temperature difference across the boundary layer. A similar indicator has not been defined yet for the case of vertical channel configurations.

The objective of the present paper is to study a spatially-developing transitional natural convective flows as a consequence of a uniform heat flux on one side of a vertical air channel of finite height. Experimental velocities and temperatures were obtained with Particle Image Velocimetry (PIV) and thermocouples respectively. The commercial software ANSYS FLUENT, in which the Vreman SGS model had been implemented as a user-defined function developed by Lau et al. [23, 24] was used to simulate the flow. For the two heat inputs investigated, an artificial inlet disturbance was used to mimic the environmental noise, inherent to experimental studies [2, 8, 19], as well as to control the triggering of the transition to turbulence within the channel. Based on the numerical and experimental time averaged velocity and

temperature distributions, transition indicators are defined. The streamwise evolution of the time-averaged velocities and temperatures, as well as the turbulence statistics are described and the ability of the different indicators to distinguish different stages of the flow transition is assessed.

It should be noted that, in recently published research [25, 26, 27], it has been demonstrated that the external thermal stratification is a confounding factor in natural convection studies in channels. For that reason it has been considered in the present work.

2. Experimental apparatus

2.1. Room and channel description

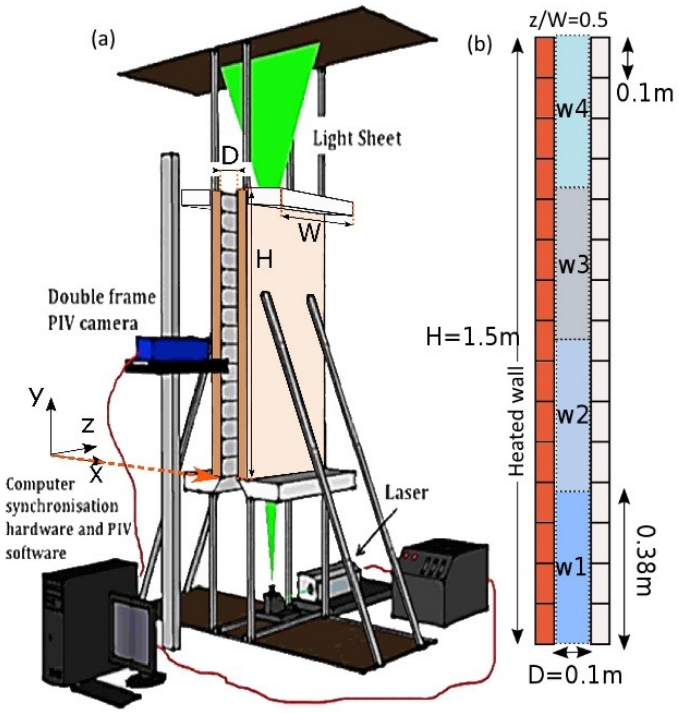

Figure 1: (a) Scheme of the experimental apparatus and coordinate system, (b) PIV fields of views at $z/W = 0.5$

The experimental apparatus has already been described in Vareilles [5], Sanvicente et al. [7] and Thebault et al. [26] so that only the main features are presented here. The apparatus was located in a 6.6 m high, 4.6 m wide and

7.0 m long laboratory. The experimental channel and the coordinate system are presented in Figure 1 (a). It consisted of two parallel vertical walls of dimensions H=1.50 m high W=0.70 m wide D=0.10 m apart, located 0.75 m above the floor. They were insulated with 12 cm thick polyurethane blocks of thermal conductivity 0.027 W/m·K. The channel was closed on both lateral sides by two vertical Plexiglas sheets to prevent lateral infiltration of air and allow optical access to the channel. The inside surface of each of the wide channel walls was covered by 15 stainless steel foil heaters, each 10 cm wide, 50 μm thick and 70 cm long. The emissivity of the foils was 0.092 and the thermal conductivity was 13 W/m·K. The leading edges of the two wide plates had 30° chamfers at the inlet in order to guide the fluid and reduce inlet turbulence. A horizontal 0.70 m $\times$ 1 m artificial ceiling was placed 75 cm above the outlet. This configuration was designed in order to have the same boundary condition above and below the channel. In the numerical model of this configuration, the presence of these wall defines the I-type configuration [28] and allows the flow to evolve freely in the extended domains therefore reducing the effect of the boundary conditions on the flow.

For temperature acquisition on the heated surface, 75 thermocouples were placed along the vertical mid-plane line $z/W = 0.5$ in which z is defined in Figure 1 (a). The thermocouples were placed inside the insulation and in contact with the heated foil. Seven thermocouples were located across the inlet and 21 thermocouples were located across the outlet, in order to obtain the mid-plane inlet and outlet temperature profiles. Finally thermocouples were located near the outlet, outside the channel. All thermocouples were standard K-types, made from 120 μm wire.

Ambient thermal conditions were evaluated with five thermocouples located at 0.1 ; 0.7 ; 1.3 ; 1.7 and 2.3 m from the floor on the same vertical pole, 1.5 m from the channel. These measurements provided the temperature distribution in the laboratory. Thermocouples measurement uncertainty was evaluated at $\pm$0.05 K.

Velocity fields on the center plane, z/W=0.5, were obtained with the Particle Image Velocimetry (PIV). The PIV system consisted of a pulsed Nd: YAG laser emitting at 532 nm. A standard set of lenses was used to transform the laser beam into light sheets and a Charge-Coupled Device (CCD) with a resolution of 540$\times$2048 pixels was used for image acquisition. The acquisition window corresponded to a 100 mm wide by 380 mm high section of the flow. This field of view covered a quarter of the channel height and thereby allowed to cover the whole height of the channel with only four

measurements. The heights at which PIV measurements were performed, namely, w1, w2, w3, w4 corresponded to the 1st, 2nd 3rd and 4th quarters of the channel respectively as shown in Figure 1 (b).

Experiments were conducted by seeding the flow with droplets of Di-Ethyl-Hexyl-Sebacat silicon oil. The particles had a diameter smaller than 1 μm and a density of 912 kg/m^2 and had sufficient light scattering capability as well as a minimal slip between the fluid and the particle [29]. The standard double frame PIV method was used in which the two images were acquired 1 ms apart. This time was set so that particles did not move by more than 1/4 of the interrogation window between the two frames. The acquisition frequency was 10 Hz.

During each measurement session, 8000 double images were acquired, which correspond to a measurement period of 14 min. This measurement period provides a reliable average of the main quantities of the flow [7]. The systematic errors, related to the laser, the seeding procedure, the camera calibration and the post processing were estimated at ± 0.015 m/s.

2.2. Experimental ambient conditions and heat losses

The experimental procedure used in each measurement session as well as the ambient room conditions have been described in details by Thebault et al. [26].

The indoor temperature distribution was recorded experimentally. For the great majority of the cases the room temperature distribution could be approximated by a linear distribution. In the numerical simulations, the stratified temperature distribution in the laboratory was therefore taken to be linear with a temperature gradient δ_T (K/m) as done by Thebault et al. [26]. A positive stratification *i.e.* temperature increasing with height, therefore corresponds to positive values of δ_T.

It was observed that for the present measurements, the temperature gradient in the laboratory increased by only 0.01 K/m per hour during any operating period. Since the measurements took approximately a quarter-of-an-hour, the temperature gradient in the room could be assumed as constant during the measurement period. The average temperature change in the room during one measurement session was ± 0.1 K. Because this change was also small, all ambient conditions could still be assumed to remain constant during the measurement period.

The channel was uniformly heated on one side and the measurements were made for two heating powers of 100 W and 230 W. The losses, through

conduction through the wall and radiation directly to the surroundings were estimated by Vareilles [5] and Sanvicente [29] at approximately 5% of the injected heat input.

The Rayleigh number Ra, defined in terms of the heat flux,q (W/m^2), and on the height of the channel, H (m), is defined as the product of the Grashof number and the Prandtl number and can therefore be expressed as

$$Ra = \frac{gbqH^4}{a\nu\kappa}, \tag{1}$$

in which g (m/s^2) is the gravitational acceleration, b (1/K) is the coefficient of thermal expansion, ν (m^2/s) is the kinematic viscosity, κ (W/m·K) is the thermal conductivity of air and a (m^2/s) is the thermal diffusivity.

The Rayleigh numbers corresponding to each heat input are shown in Table 1. The ranges of external thermal stratification observed experimentally for each Rayleigh number is also indicated for information purposes.

Table 1: Summary of the cases studied

Cases	100 W	230 W
Ra	1.5×10^{12}	3.5×10^{12}
Electrical power Q_t (W)	100	230
Net heat input Q (W)	95	219
Net heat flux q (W/m^2)	90	208
Exp. range of δ_T (K/m)	0.5–1.1	0.3–1.4

3. Numerical methodology

The computational domain is illustrated in Figure 2. Based on the I-type geometry defined by Manca et al. [28], and as was done by Lau et al. [16], two domains were added to the lower and upper ends of the channel through which air flowed into and out of the channel. The top boundary is located 0.75 m above the channel outlet and corresponds to the artificial ceiling present in the experimental apparatus. It was modeled as an impermeable no slip wall. A uniform heat flux was imposed at the heated wall. The other walls, plotted by a thick plain black line, were set as adiabatic except for the when specified otherwise.

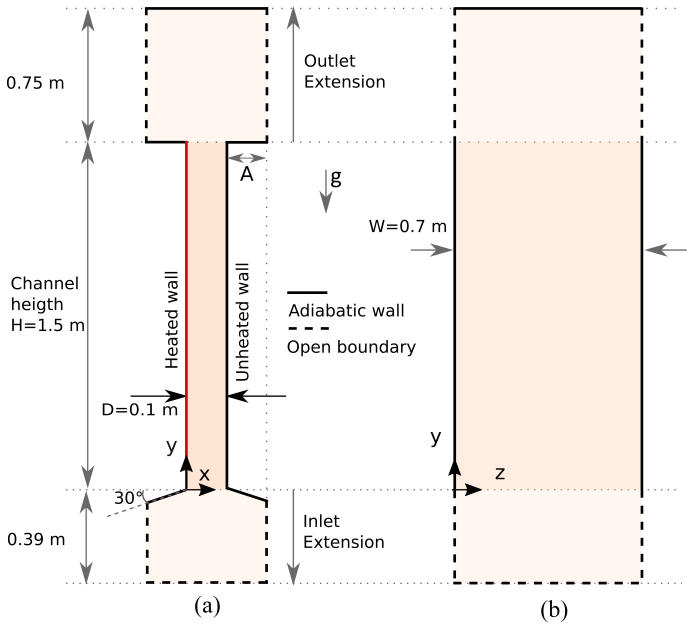

Figure 2: Scheme of the computational domain (a) elevation (b) side elevation

3.1. Large-Eddy Simulation and Vreman SGS model

In the LES formulation, the flow is separated into large and small scales based on a spatial filtering. The filter size is commonly assumed to be equal to the size of the computational grid. The large scale motions are directly simulated whereas a SGS model is used to evaluate the effects of flow structures smaller than the filter size used in the simulations.

The grid-filtering operation is defined for a physical quantity φ as

$$\overline{\varphi}(\mathbf{x},t) = \int_{\mho} \omega(\mathbf{x}-\mathbf{x}')\varphi(\mathbf{x}',t)d\mathbf{x}' \tag{2}$$

in which $\mathbf{x} = (x, y, z)$ is the spatial coordinate, t the time, $\mho$ is the computational domain, ω is a normalized filter function, defined here as a box filter, of width Δ.

Because in natural convection, the changes in density, ρ (kg/m^3), can be significant, it is common to adopt a modified approach for the filtering of the Navier-Stokes equations, commonly called the Favre-filtering, defined as

$$\widetilde{\varphi}(\mathbf{x},t) = \frac{\overline{\rho\varphi(\mathbf{x},t)}}{\overline{\rho}} \tag{3}$$

in which the operator $\sim$ indicates the Favre-filtered quantity.

The instantaneous variable can now be expressed as

$$\varphi(\mathbf{x},t) = \widetilde{\varphi}(\mathbf{x},t) + \varphi''(\mathbf{x},t), \tag{4}$$

in which $\widetilde{\varphi}(\mathbf{x},t)$ represents the quantity that will be directly calculated whereas $\varphi''(\mathbf{x},t)$ represents the part of the component, smaller than the grid filter width, that will be modeled by the SGS.

The resulting set of conservation equations for a buoyancy-driven flow at low-Mach-number using Favre averaging, written in tensor form with the Einstein summation convention may be written as :

conservation of mass,

$$\frac{\partial \overline{\rho}}{\partial t} + \frac{\partial(\overline{\rho}\widetilde{u}_i)}{\partial x_i} = 0, \tag{5}$$

conservation of momentum,

$$\frac{\partial\left(\overline{\rho}\widetilde{u}_j\right)}{\partial t} + \frac{\partial\left(\overline{\rho}\widetilde{u}_i\widetilde{u}_j\right)}{\partial x_i} = -\frac{\partial \overline{p}}{\partial x_j} + \frac{\partial \widetilde{\sigma}_{ij}}{\partial x_i} + \frac{\partial \tau_{u_i u_j}}{\partial x_i} + (\overline{\rho} - \rho_0)g_j, \tag{6}$$

and conservation of energy,

$$\frac{\partial\left(\overline{\rho}C_p\widetilde{T}\right)}{\partial t} + \frac{\partial\left(\overline{\rho}C_p\widetilde{u}_i\widetilde{T}\right)}{\partial x_i} = \frac{\partial}{\partial x_i}\left(\kappa\frac{\partial \widetilde{T}}{\partial x_i}\right) + \frac{\partial\left(C_p\tau_{u_iT}\right)}{\partial x_i}. \tag{7}$$

$\widetilde{u}_i$ (m/s) are the Cartesian velocity components, ρ_0 is the reference density at the reference temperature T_0 (K). $\overline{\rho}$ and $\widetilde{T}$ are respectively the density and the temperature, $\overline{p}$ (Pa) is the dynamic pressure and C_p ($\mathrm{m}^2\cdot\,\mathrm{kg}\cdot\,\mathrm{s}^{-2}\cdot\,\mathrm{K}^{-1}$) is the specific heat capacity at constant pressure. $\widetilde{\sigma}_{ij}$ is the stress tensor which can be written, under the Stokes assumption as

$$\widetilde{\sigma}_{ij} = 2\eta\left(\widetilde{Sr}_{ij} - \widetilde{Sr}_{kk}\delta_{ij}\right), \tag{8}$$

where $\widetilde{Sr}_{ij}$ is the rate of strain tensor, η the dynamic viscosity and δ_{ij} is the Kronecker delta,

$$\widetilde{Sr}_{ij} = \frac{1}{2}\left(\frac{\partial \widetilde{u}_i}{\partial \widetilde{x}_j} + \frac{\partial \widetilde{u}_j}{\partial \widetilde{x}_i}\right). \tag{9}$$

The effect of the non-simulated small-scale structures is represented by the SGS stress tensor $\tau_{u_iu_j}$ and the SGS heat flux vector τ_{u_iT} in equations

6 and 7. To describe these quantities, the Vreman SGS model [30] adapted by Lau [31] to transition natural convection flows with low turbulence level is used in this work. It has been shown that in natural convection problem in cavities [23] and channel flows [11, 16, 24], this SGS model yields better agreement with experiment than the Smagorinsky SGS model [32].

The subgrid Reynolds stresses and turbulent heat fluxes are represented in the Vreman SGS model as

$$\tau_{u_i u_j} = -2\eta_{sgs}\left(\widetilde{Sr}_{ij} - \frac{1}{3}\widetilde{Sr}_{kk}\delta_{ij}\right), \tag{10}$$

and

$$\tau_{u_i T} = \frac{\eta_{sgs}}{Pr_{sgs}}\frac{\partial \widetilde{T}}{\partial x_i} \tag{11}$$

in which η_{sgs} is calculated based on the SGS viscosity model proposed by Vreman [30], namely,

$$\eta_{sgs} = \overline{\rho} C_{sgs}\sqrt{\frac{B_d}{c_{ij}c_{ij}}}, \tag{12}$$

Pr_{sgs} and C_{sgs} are coefficients of the SGS model and $c_{ij} = \partial\widetilde{u}_j/\partial x_i$, $B_d = \widetilde{d}_{11}\widetilde{d}_{11} - \widetilde{d}_{12}^2 + \widetilde{d}_{11}\widetilde{d}_{33} - \widetilde{d}_{13}^2 + \widetilde{d}_{32}\widetilde{d}_{33} - \widetilde{d}_{23}^2$ and $\widetilde{d}_{ij} = \Delta_m^2 c_{mi}c_{mj}$, Δ_m being the filter width in the m direction. As suggested by Vreman [30], C_{sgs} and Pr_{sgs} were set to 0.1 and 0.4 respectively. In the remainder of this work, only filtered quantities are considered and the overbars $\sim$ and $-$ will not be used for the sake of clarity. The derivation of the LES approach the implementation of the Vreman SGS model and its validation for this type of flow is presented in detail in the work by Lau [31].

Vreman SGS was particularly suitable for simulations of transitional flows as it allows a vanishing dissipation in laminar regions of the flow [23]. This model has been validated against experimental data for various configurations, such as a cavity flow [23] or the channel flow of Miyamoto et al. [2] simulated by Lau et al. [11, 24]. More recently, Li et al. [12] compared the results obtained with a LES solver with a Vreman SGS and the experimental results of Miyamoto et al. [2] with their own results obtained with a Direct Numerical Simulation (DNS). Both LES and DNS codes were able to accurately predict the time averaged velocities and turbulent intensity in the

high part of the channel (no comparison were shown at lower levels). The LES data even provided more accurate prediction of the time averaged excess wall temperature. Li et al. [12] explained this unexpected outcomes by differences in the boundary conditions. However both the LES and DNS accurately predicted the height at which transition occurred which is one of the most crucial points in the present work.

In the remainder of the paper, the x and y components of the velocity (see Fig.2 for the coordinate system) will correspond to the u and v components of the velocity, also mentioned as respectively the wall normal and the streamwise components of the velocity.

3.2. Boundary conditions

In numerical studies about natural convection flow generated in open vertical channel, the problem of the modeling of the boundary condition is considered as one of the most difficult. Indeed, in most case in mixed or forced convection, the mass flow rate condition is a large fixed value known in advance and therefore the inlet conditions can be easily modeled. In purely driven natural convection through finite-size open channels, the flow is weak and its characteristics depend on a complex interaction between the generated natural convection flow and the boundary conditions.

For a more extensive review of the issues that have been encountered in the numerical modeling of the open boundary conditions as well as the strategies that were developed in an attempt to model them we refer to p.21-29 of Thebault [19].

3.2.1. Thermal and pressure stratifications at the openings

As was observed experimentally by Thebault et al. [26], the ambient temperature, in the far-field was linear so that at any height in the surrounding ambient atmosphere the temperature is,

$$T_a(y) = T_0 + (y - y_0)\,\delta_T, \tag{13}$$

The subscript a refers to a quantity taken in the far-field, and δ_T is the temperature gradient in the far-field. The external temperature gradient δ_T is positive if the temperature increases upwards and negative if it decreases. The ambient atmosphere is considered as a stationary, single phase ideal gas so that the ideal gas law and the hydrodynamic stability law can be applied viz,

$$p_a = \rho R_{air} T_a, \tag{14}$$

$$\frac{dp_a}{dy} = -\rho g. \tag{15}$$

in which ρ is the density of air and R_{air} (J/kg^{-1}K^{-1}) is the specific gas constant. By substituting equation (13) in equation (14) and then substituting ρ in equation (15) and integrating, it follows that the hydrostatic pressure follows the exponential law

$$p_a(y) = p_0 \left(1 + \frac{\delta_T}{T_0}(y - y_0)\right)^{\left(\frac{-g}{R_{air}\delta_T}\right)}. \tag{16}$$

In the computational model, these temperature and pressure distributions are applied at the open boundaries (see Figure 2 for the location of the open boundaries) of the computational domain using a user-defined function. The stratified temperature equation (13) defines the temperature of the fluid entering the open boundaries.

In the final numerical model which is used to generate the numerical results studied here, the temperature $T_{in,num}$ of the fluid entering the channel itself has a temperature of

$$T_{in,num}(y) = T_0 - 0.23H\delta_T, \tag{17}$$

which is very close to the experimental inlet temperature that was measured on the same apparatus by Thebault et al. [26] at

$$T_{in,exp}(y) = T_0 - 0.25H\delta_T. \tag{18}$$

3.2.2. Inlet noise

It is currently impossible to exactly represent noises and disturbances emanating from the laboratory environment, as the flow enters the channel. However, as mentioned in the introduction, in experimental works, significant velocity perturbations were reported to enter in the channel from the laboratory environment [2, 8, 19]. These disturbances needed to be introduced in the velocity field at the inlet of the computational domains by Fedorov and Viskanta [10], Lau et al. [16], Tkachenko et al. [17] so as to match experimental data. To that end, the environmental noise in the room is modeled here as a disturbance of the velocity components generated at entrance of

the computational domain by the Spectral Synthesizer method, based on the work of Smirnov et al. [33] and implemented in ANSYS FLUENT. This method generates a random spatial and temporal coherent noise at the lower open-boundaries of the computational domain (Fig. 2), and is one of the most commonly-used method to synthesize disturbed inlet conditions for LES simulations [34].

As can be seen in Fig. 3 this method leads to a reasonable representation of the experimentally recorded turbulent intensity in the inlet region of the channel. In the present study, the inlet turbulence intensity ranged between 15 to 20%; of the same order as used by Fedorov and Viskanta [10].

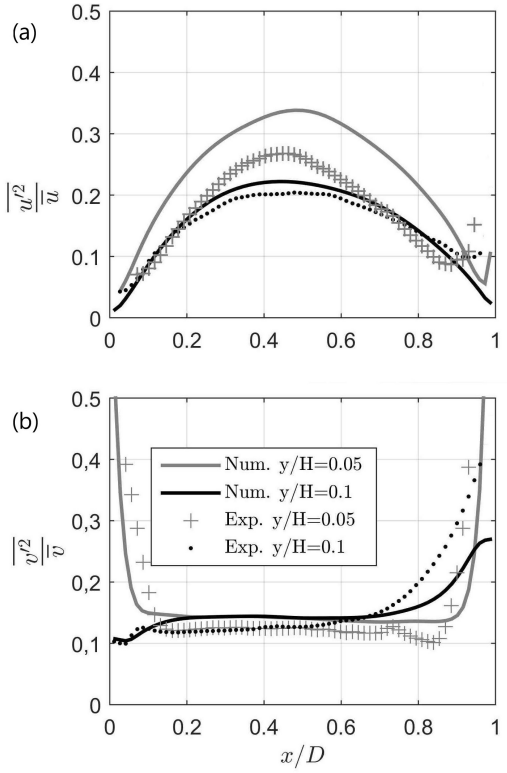

Figure 3: Experimental and numerical (a) wall-normal (u) and (b) streamwise (v) turbulent intensities in the inlet region of the channel. Solid lines, numerical data; dotted lines, experimental data.

3.2.3. Wall-to-wall radiation

Only one wall is directly heated by the Joule effect in the experiments. The wall facing the heated wall is "passively" warmed by radiation so that these walls are referred to as the heated wall and the unheated wall respectively. The same nomenclature is adopted for the walls in the numerical model.

Using the radiosity model and considering air to be a non-participative medium, Sanvicente [29], estimated that approximately 10% of the total net heat injected into the channel was transmitted by radiation to the unheated wall for the same configuration as used in this study. As a consequence, in the numerical model, the total heat flux injected in the channel follows the same distribution, namely, 90% of the injected heat is given to the heated wall and 10% to the unheated wall. This approach constitutes the simplest approximation that allows radiation heat transfer to be taken into account without the need for calculating radiative heat transfer exchanges in the computational model; thereby considerably reducing the computation burden.

3.3. Mesh and domain validations

A mesh convergence study was then conducted. The test case corresponds to the higher Rayleigh number, $Ra = 3.5 \times 10^{12}$, with an external thermal stratification of $\delta_T = 0.72$, which corresponds to one of the average thermal stratification that was observed experimentally (see Table 1).

Four mesh sizes were used, a very coarse mesh (VCM) of $\sim 500 \times 10^3$ nodes, a coarse mesh (CM) of $\sim 800 \times 10^3$ nodes, an intermediate mesh (IM) of $\sim 1.5 \times 10^6$ nodes and a fine mesh (FM) of $\sim 2.3 \times 10^6$. The meshs are ordered in the x,y and z direction with inflation at the walls. Details of each mesh are presented in Table 2.

Table 2: Mesh characteristics within the channel itself

Name	Elements in $x \times y \times z$	Number of elements
VCM	55×135×65	$\sim 500 \times 10^3$
CM	60×165×80	$\sim 800 \times 10^3$
IM	75×240×85	$\sim 1.5 \times 10^6$
FM	90×300×85	$\sim 2.3 \times 10^6$

The size of the extended domain was of A=7cm (Fig. 2). The calculation was initialized with a quiescent fluid in the whole domain i.e. zero initial velocity in the domain and at the boundaries. The temperature in the whole

domain was of T_0. At the open boundaries the boundary conditions of a thermally stratified ambient are applied (section 3.2.1) i.e. the temperature and pressure conditions are those of equations 13 and 14. At the walls 90% of the total heat flux is imposed at the heated wall, and 10% of the remaining heat flux is imposed at unheated wall in order to model the wall to wall radiation exchange as mentioned in section 3.2.3. The other walls are adiabatic. The walls have a no-slip condition.

After the first few iterations, complex structures are seen and approximately 20 to 30 s are needed in order to obtain an established ascendant flow. From this point, the mass flow rate was still fluctuating but the maximum difference observed between its maximum and minimum values was less than 30% of the minimum. Averaging for the flow statistics was only commenced after 100 simulation seconds had elapsed. The duration of the sampling period, in order to obtain statistical convergence of the mean values to an accuracy greater than 1%, was another 100 s. In what follows, the time-averaged quantities will be indicated by an overline $(-)$.

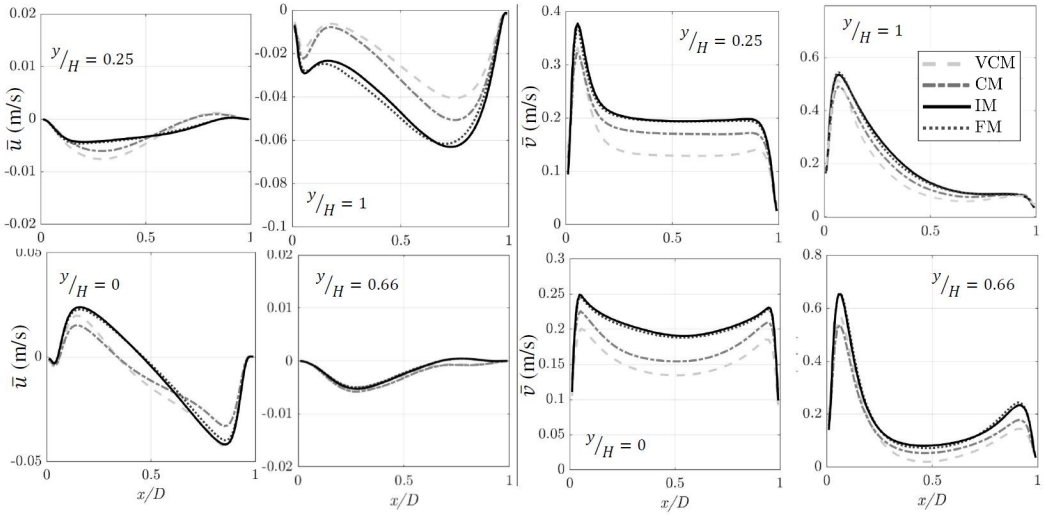

Figure 4: Time-averaged velocities distributions for the different mesh sizes at $Ra = 3.5 \times 10^{12}$ in the mid plan $z/W = 0.5$. The four figures on the left are the wall-normal time-averaged velocities $\overline{u}$ at four different locations respectively $y/H = [0, 0.25, 0.66, 1]$, the four figures on the right are the time-averaged streamwise velocities $\overline{v}$ plotted at the same elevations as that for $\overline{u}$

As is shown in Fig. 4, there are very small differences, $< 1\%$, in the time-averaged velocity profiles between the IM and the FM grids. The temperature

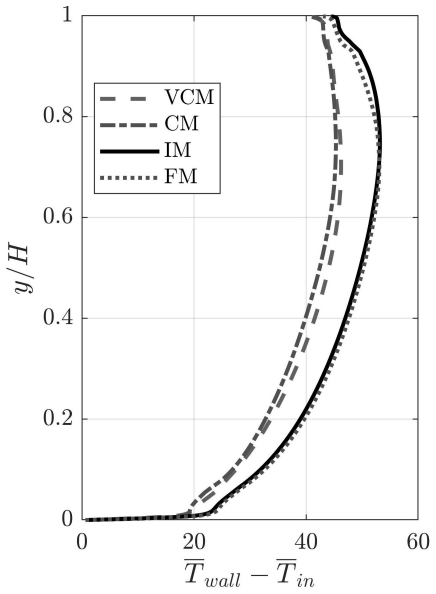

Figure 5: Wall-temperature distributions for the different mesh sizes at $Ra = 3.5 \times 10^{12}$

profiles at the wall in Fig. 5 are also very similar for these two meshes with differences $< 1\%$ except at the very top of the channel where a difference of 4% is reached. Multiplying the number of elements by 1.533 has almost no effect on the time averaged quantities, therefore the IM grid was considered a satisfactory mesh for the present study. A slice of the mesh at mid-height of the middle section of the channel $z/W = 0.5$, $y/H \in [0.50, 0.54]$ is displayed in Figure 6.

The y-plus value of the first node in the wall normal-direction was calcu-

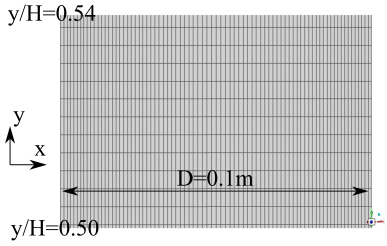

Figure 6: IM mesh in the section $z/W = 0.5$ at mid height

lated as follows

$$x^+ = \frac{v_* x}{\nu}, \tag{19}$$

in which v_* is the friction velocity at the nearest wall and where x was taken as the size of the first grid node in the wall-normal direction. A maximum y-plus value of $x^+ = 0.8$ was obtained by using the maximum friction velocity, implying that viscous sub-layer had been sufficiently resolved. In the literature, similar grid resolutions have been used in numerical LES modeling of natural convection for which the transitional behavior of the flow was shown to be correctly modeled (see e.g.[13], [23] [17]).

Now that the mesh has been validated, the influence of the inlet and outlet extensions sizes is briefly discussed. The sizes of the extended domains were progressively increased by modifying the size of A, in Fig. 7, on both sides of the channel. Four values of A were studied, D_0, the initial extended domain had a value of A =7 cm, whereas D_1, D_2 and D_3 had values of A equal to 14, 21 and 28 cm respectively. The mesh remained unchanged in the channel and in the initial extended domain D_0 with additional cells being added in further extensions.

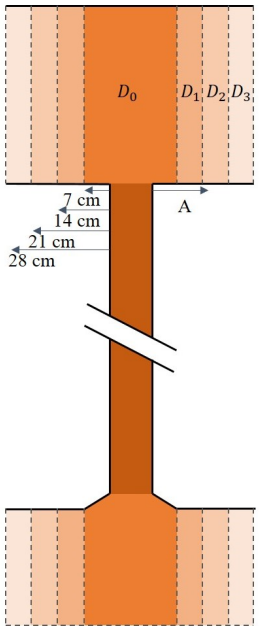

Figure 7: Representation of the different computational domains for various sizes of A. Thick black line represents walls and dashed lines represents open boundaries.

As may be seen in Fig. 8, the size of the extended domain have an impact on the mass flow rate. However, the changes in the mass flow rate were around 2% between D_1 and D_2 at $Ra = 1.5 \times 10^{12}$ and were almost insignificant between D_2 and D_3 at $Ra = 3.5 \times 10^{12}$ case. This is the reason for choosing domain D_1 for $Ra = 1.5 \times 10^{12}$ and D_2 for $Ra = 3.5 \times 10^{12}$.

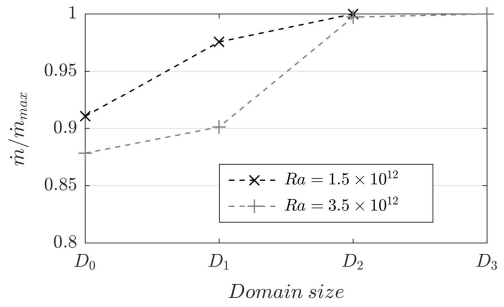

Figure 8: Influence of the extended domain size on the mass flow rate.

3.4. Numerical experimental confrontation

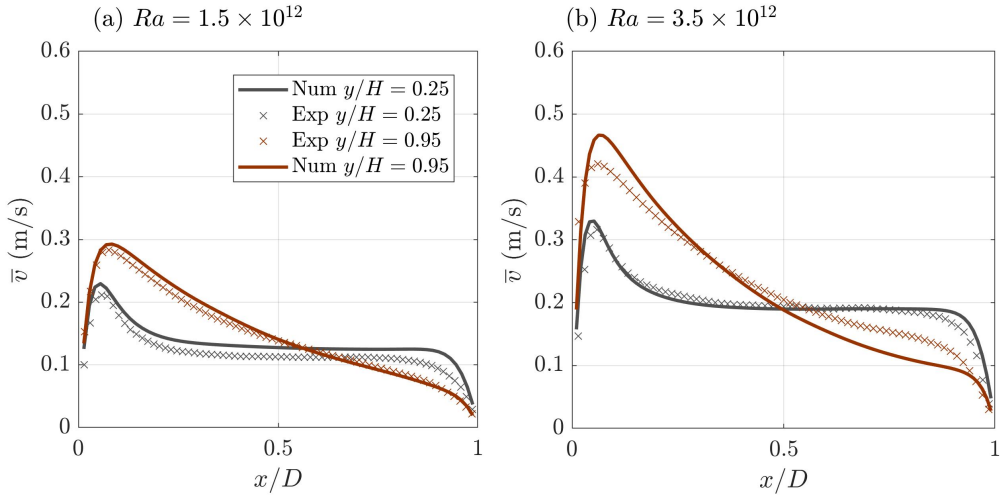

Figure 9: Streamwise time-averaged velocity in the lower region at $y/H = 0.25$ and in the upper region at $y/H = 0.95$. (a) $Ra = 1.5 \times 10^{12}$ (b) $Ra = 3.5 \times 10^{12}$. Continuous lines indicates the numerical results whereas the symbol indicates the experimental results

Now that the numerical model, mesh and domain have been validated, it is confronted to experimental data. Numerical and experimental time averaged streamwise velocity profiles in the lower and upper regions of the channel have been plotted for the two cases considered here in Fig. 9. It can be observed that there is a reasonable agreement between the experimental and numerical data, with higher differences in the case of $Ra = 3.5 \times 10^{12}$ in the higher region of the channel.

It is important to note that the agreement between the experimental and numerical results has never been reached for this type of configuration [10], [16], [12] or [17]. The best reported agreements remain probably those of the numerical LES model of Lau et al. [11] with the experimental results of Miyamoto et al. [2]. In the present work, the same LES methodology is used, only the geometry was changed.

However, despite this difficulty to achieve numerical experimental agreement, it never prevented the numerical model to be used to provide new insights on the flow characteristics. For that reason, it is not the ambition of the present paper to achieve a better agreement with experimental data than those previously obtained. The ambition here is to observe similar trends and indicators of the transition between the experimental and numerical results.

4. Transition indicators and flow development

The study presented in this paper focuses on two cases corresponding to two Rayleigh numbers. The main discussion deals with the experimental and the numerical results at $Ra = 3.5 \times 10^{12}$ and is extended to the numerical results and some experimental data at $Ra = 1.5 \times 10^{12}$.

During the experimental measurements, at $Ra = 3.5 \times 10^{12}$, velocity recordings were performed over the whole height of the channel for an external thermal stratification between 1.39 K/m and 1.40 K/m. It therefore reduced the repeatability issues between the measurements due to the external thermal stratification to non-appreciable differences. As a consequence, an external thermal stratification of δ_T=1.4 K/m was simulated in the numerical case at $Ra = 3.5 \times 10^{12}$. A similar stability in the experimental results could not be achieved at $Ra = 1.5 \times 10^{12}$. As a consequence, only partial development of the flow is presented at $Ra = 1.5 \times 10^{12}$ and a thermal stratification of δ_T=1.1 K/m which corresponded to the highest stratification experimentally recorded at this Rayleigh number as reported in Table 1. The same thermal stratification was used in the numerical simulation at $Ra = 1.5 \times 10^{12}$.

In what follows, the temperatures will be expressed as the temperature rise above the reference temperature T_0 and is denoted as θ viz,

$$\theta = T - T_0. \tag{20}$$

For each case, the reference temperature, T_0, is defined as the temperature far from the channel at the height of the inlet to the channel. When needed the air properties are taken at T_0. In the numerical simulations $T_0 = 293.15$ K.

In what follows, different transition indicators are proposed and their usefulness as indicators of flow development is assessed. These discussions are as much as possible supported by both our experimental and numerical data. However, no measurement of the fluid temperature inside the channel has been performed. Thus, in the case this information is needed, experimental work from the literature are used to support the discussions.

Note that for a better readability it has been decided in some cases to present the results over a restricted range around the region of interest, which is around the indicator under study, this range can be different depending on the available data, the Rayleigh numbers, the phenomenon to be observed or between the experimental and numerical results.

4.1. Wall-temperature indicator, h_T

In studies of natural convection in uniformly heated vertical channels, it is common to use the first local maximum, reached by the temperature at the heated-wall, in order to localize the transition region, as was done by Miyamoto et al. [2] and many other researchers mentioned in the introduction. One of the reasons is the ease to obtain measurements of the temperature distribution at the wall compared to velocity measurements in the fluid.

The same definition will be used for this indicator in the present work and its streamwise location will be referred to in its non-dimensional form as h_T.

The wall temperature distributions, $\overline{\theta}^*_{wall}$, at $Ra = 3.5 \times 10^{12}$ have been plotted for the numerical case in Fig. 10 and for the experimental case in Fig. 11. The streamwise evolution of the minimum temperature in the bulk $\overline{\theta}^*_{min}$ is also displayed for the numerical case in Fig. 10. All the quantities were scaled with their maximum streamwise value for visualization purposes. The scaled quantities are indicated by the superscript $*$.

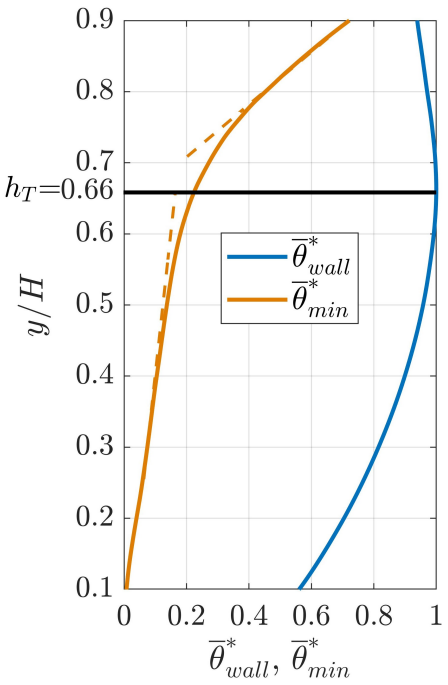

Figure 10: Streamwise evolution of numerically obtained $\overline{\theta}^*_{wall}$ and $\overline{\theta}^*_{min}$. Thin dashed lines have been plotted to indicate linear trends or significant changes in the quantities growth, the plain black line plots h_T.

The temperature at the wall $\overline{\theta}^*_{wall}$ increases from the beginning of the channel and reaches a local maximum at $y/H = 0.66$ in the numerical case and at $y/H = 0.45$ in the experimental case which correspond to h_T.

Regarding the minimum temperature in the fluid $\overline{\theta}^*_{min}$ in Fig. 10, it rises slowly and almost linearly from approximately $y/H = 0.1$ to $y/H = 0.5$. This increase of temperature is mainly due to conduction, diffusion and weak wall-normal convective transfers. Around $y/H \simeq 0.5$, the rate in slope of $\overline{\theta}^*_{min}$ changes and above h_T, $\overline{\theta}^*_{min}$ starts to significantly increase. From $y/H = 0.8$, $\overline{\theta}^*_{min}$ evolves almost linearly with a higher rate than that in the lower part of the channel. The sudden increase of $\overline{\theta}^*_{min}$ above h_T translates an increase of the heat transfer toward the bulk region and therefore a transition. However, as showed by the dashed lines, the variation of slope of $\overline{\theta}^*_{min}$ suggests that some transition phenomena have started below h_T.

The evolution of the numerically obtained temperature profiles in the

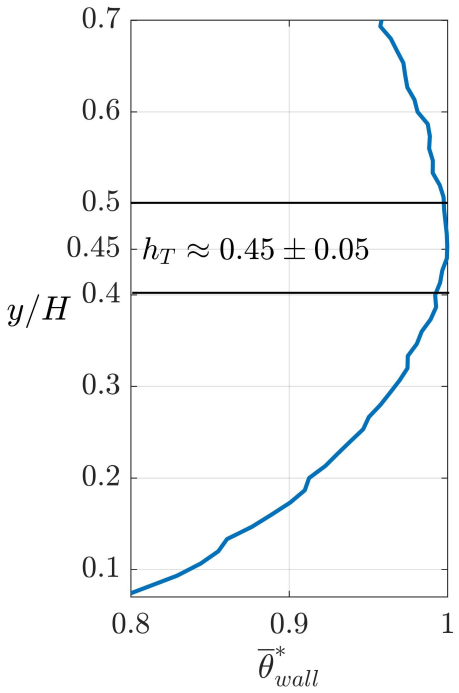

Figure 11: Streamwise evolution of experimentally measured $\overline{\theta}^*_{wall}$. The plain black line plots h_T

fluid at $Ra = 3.5 \times 10^{12}$ have been plotted in Fig. 12 (a). Two color sets are used, the light purple/dark purple set is used for the profiles plotted below h_T and the yellow/red colors are used for the profiles plotted above it. Below h_T the hot fluid remains close to the walls in what could be defined as the thermal boundary layer. The temperature in the bulk region remains almost at inlet temperature despite a very slight increase. Then, from h_T the wall temperature decreases. Moreover by continuity in the wall-normal direction, the temperature of the fluid in the vicinity of the wall, here between the wall and $x/D \simeq 0.03$ decreases as well. Away from this region, in the central part of the channel, the fluid temperature, which remained almost at the inlet temperature in the two first thirds of the channel, below h_T, starts to significantly increase from $\overline{\theta}^* = 0.01$ to $\overline{\theta}^* \simeq 0.15 - 0.20$ in the last third of the channel.

No experimental detailed measurements of the fluid temperature spatial development were performed in the present work. However the time aver-

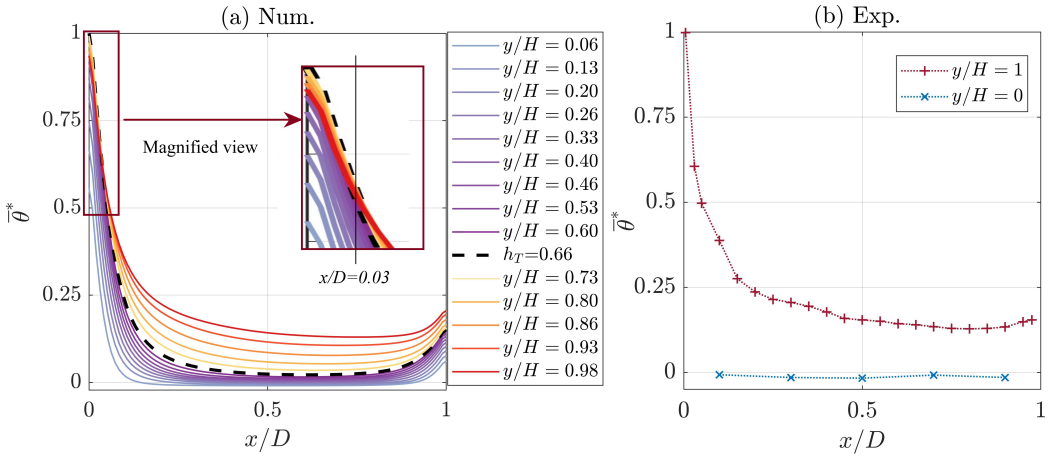

Figure 12: Temperature profiles in the fluid at $Ra = 3.5 \times 10^{12}$, $z/W = 0.5$, (a) Numerical, The thick dashed line plots the temperature profiles at h_T (b) Experimental.

aged inlet and outlet temperatures experimentally obtained for the Rayleigh number of $Ra = 3.5 \times 10^{12}$ are plotted in Fig. 12 (b). The outlet temperature in the bulk region reaches 10 to 20% of that of the maximum temperature at the wall which is consistent with the numerical results. Moreover, the increase of fluid temperature in the bulk of the flow observed around h_T is consistent with all the experimental studies in which both the wall and fluid temperatures are presented (see e.g. [2], [4]). Furthermore some studies in which temperatures measurements in the fluid were carried with a relatively high spatial resolution, [3], [9] and [27] show that there is a jump in the fluid temperature from h_T which entirely support the above numerical observations. As for the decrease of temperature in the vicinity of the wall, that is observed numerically above h_T in Fig. 12 (a), it can be experimentally supported by the experimental wall temperature in Fig. 11. Indeed, by continuity in the wall-normal direction, the fluid, in a certain region near the wall, follows the same temperature variations as those observed at the wall. Therefore, despite no temperatures in the fluid were measured in the present work, the decrease of the experimental wall temperature presented in Fig. 11 imply that in a certain region of the fluid, near the wall, the temperature also decreases.

These numerical and experimental results show that there is a transition, characterized by significant changes in the mean temperature fields, which is

adequately indicated by h_T.

4.2. Velocity indicator, h_v

The velocity indicator defined here reproduces a similar indicator that was defined and used in the scaling analysis of Li et al. [27] and in the experimental work of Daverat et al. [9]. Their configuration was this of a symmetrically heated vertical water channel.

In their work they partitioned the flow into different zones. Among them they observed that, before transition occurs and because of the constant heat injection at the wall, a high velocity buoyant region is generated near the heated wall and the fluid in that region is accelerated in the streamwise direction. Concomitantly with this increase and by mass conservation, the streamwise velocity of the fluid in the bulk of the channel is decreasing.

Based on this work by Li et al. [27], the region where $\partial\overline{v}/\partial y > 0$ which corresponds to the accelerating buoyant region will be referred to as the Natural Convection Boundary Layer (NCBL). The region where $\partial\overline{v}/\partial y < 0$, which corresponds to the decelerating region, will be referred to as the Bulk Region (BR). These regions have been illustrated on the present evolution of the streamwise numerical velocities in the lower part of the channel, in Fig. 13.

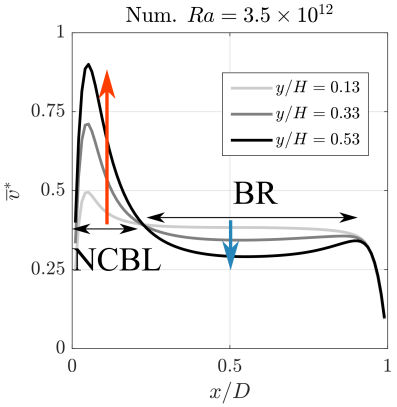

Figure 13: Illustration of the NCBL and BR zones, as they are defined by Li et al. [27], on the streamwise velocity profiles in the lower part of the channel. The ascending orange arrow indicates the accelerating trend of the fluid in the NCBL whereas the blue descending arrow indicates the decelerating trend in the BR.

However they observed that these trends were inverted after a certain elevation i.e. the velocity difference, $\Delta\overline{v}$ between the peak velocity in the

NCBL and the velocity in the BR reached a maximum and started to decrease above a certain height. They associated this change to a drastic increase of the momentum transfer from the near wall region to the bulk region and therefore to transition. The maximum of $\Delta\overline{v}$ was therefore used in their work as the transition indicator.

A similar indicator h_v is reproduced here. Similarly to their work h_v is defined as the height at which the maximum of

$$\Delta\overline{v}(y/H) = \overline{v}_{max}(y/H) - \overline{v}_{bulk}(y/H) \tag{21}$$

is reached. $\overline{v}_{max}$ is the maximum of the streamwise velocity evaluated at each streamwise position and $\overline{v}_{bulk}$ is the streamwise velocity in the bulk of the flow.

In the case of Daverat et al. [9] and Li et al. [27] the channel was heated on both sides, so that the bulk velocity was taken in the center of the channel, at mid-distance from each heated plate. In the present work, only one wall is heated so that there are no symmetry anymore and the definition of the bulk velocity is more difficult. The bulk velocity needs to be evaluated, in the BR, out of the laminar NCBL which length, defined above, will be noted in its non-dimensional form as δ_{NCBL}. In the present work, δ_{NCBL} remains within the range $x/D \in [0.2; 0.35]$ and therefore the middle of the channel, at $x/D = 0.5$ remains out of the NCBL so that it can also be considered as a suitable location to evaluate the bulk flow velocity.

The streamwise evolutions of $\overline{v}^*_{max}$, $\overline{v}^*_{bulk}$ and $\Delta\overline{v}$ are plotted in Fig. 14 for the numerical case and in Fig. 15 for the experimental case.

In the numerical case, in Fig. 14, $\overline{v}^*_{max}$ and $\Delta\overline{v}$ increase almost linearly from $y/H = 0.30$ to $y/H = 0.5$. $\Delta\overline{v}$ reaches its maximum at $y/H = 0.71$ and $\overline{v}^*_{max}$ slightly higher at $y/H = 0.72$. $\overline{v}^*_{bulk}$ reaches a minimum a little bit lower. As mentioned above, the height at which $\Delta\overline{v}$ is reached will be referred to in its non-dimensional form as h_v and is located higher than h_T.

As for the experimental case, the streamwise evolution of the velocity is similar to what was observed numerically in the lower part of the channel, $\Delta\overline{v}$ and $\overline{v}^*_{max}$ rise almost linearly from y/H=0.1 to $y/H \approx 0.3$. Then $\Delta\overline{v}$ reaches a maximum at $h_v \simeq 0.44 \pm 0.04$. $\overline{v}^*_{max}$ also reaches a local maximum around $y/H = 0.45$ however the decrease that follows is very light and $\overline{v}^*_{max}$ start increasing again above y/H=0.50.

In general, there is agreement in the trends before and above h_v between the numerical and experimental results. The only difference being for $\overline{v}^*_{max}$ which start increasing again in the experiment from $y/H = 0.5$.

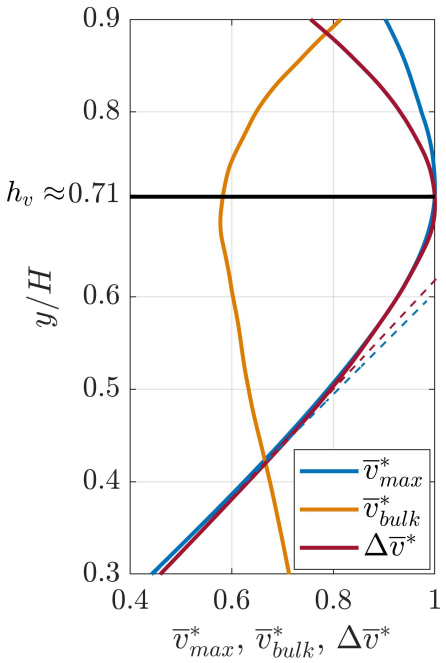

Figure 14: Streamwise evolution of numerically obtained $\Delta\overline{v}$, $\overline{v}^*_{max}$ and $\overline{v}^*_{bulk}$. Thin dashed lines have been plotted to indicate linear trends and significant changes in the quantities rate of growth. The plain black line indicates h_v

One of the explanation for this difference could be the presence of an intermittent reverse flow that has been reported to occur for these configurations at this Rayleigh number [7, 35]. Indeed, it should be noted that in the experimental results, h_v is reached lower ($y/H = 0.44$) than in the numerical results ($y/H = 0.71$). Because the present channel is of finite size there may be the influence of a reverse flow, entering from the channel outlet which would reduce the numerical velocity, whereas in the experimental case, h_v is too low in the channel to be affected by this reverse flow.

Note that in the case of a long enough channel, the increase of velocity, a certain distance after h_v, could be expected. Indeed, because of the isoflux condition the temperature generally increases in the channel as the height increases. Consequently the density of the fluid is expected to keep decreasing and therefore by mass conservation the velocity to increase. However, due to the lack of experimental data in the literature about detailed spatial de-

velopment of the flow, this phenomenon has not been reported yet. Despite only hypothetical explanations can be provided to explain this difference in trends, the numerically observed decrease of v_{max} is consistent with other experimental observations. Indeed, the decreased in v_{max} above h_v is more pronounced for the experimental results at $Ra = 1.5 \times 10^{12}$ as it will be showed in section 4.4. Finally, the decrease of v_{max} above h_v is clearly visible in experimental results of Daverat et al. [9]. These experimental results support the numerical trend that is observed here for v_{max} above h_v.

Because of the experimental measurement noise and uncertainties, it is difficult to assess experimentally which of h_T or h_v is located lower or if they are at the same elevation. However they remain very close.

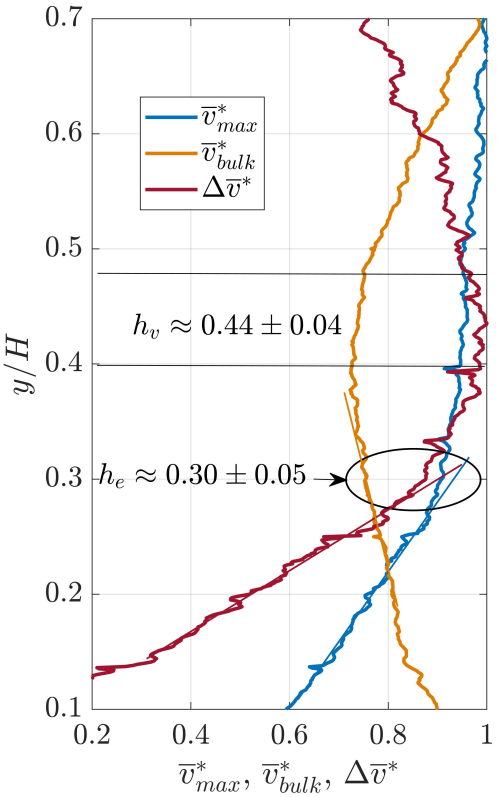

Figure 15: Streamwise evolution of experimentally measured $\Delta\overline{v}$, $\overline{v}^*_{max}$ and $\overline{v}^*_{bulk}$. Thin dashed lines have been plotted to indicate linear trends and significant changes in the quantities rate of growth. Two horizontal blacks line indicate the location of h_v. An ellipse is used to indicate the approximative location of h_e.

Streamwise velocity profiles for the Rayleigh number of $Ra = 3.5 \times 10^{12}$ and at different elevation are plotted in the mid-plane z/W=0.5, in Fig. 16 for the numerical case and in Fig. 17 for the experimental case. Two color sets are used in each figure. The light blue/dark blue set is used for the profiles plotted below h_v and the orange/red colors are used for the profiles plotted above it.

At the entrance the velocity profile is almost flat. Then as the altitude increases and up to h_v, the flow in the NCBL is accelerated, whereas the velocity in the BR decreases because of the mass conservation. Above h_v the flow undergoes drastic changes; the high velocity region broaden due to turbulent transfers and tends to progressively encompass the whole channel width.

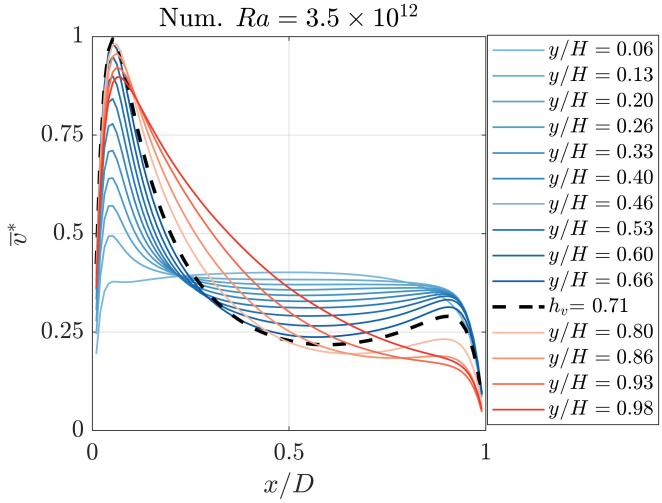

Figure 16: Numerically obtained velocity profiles at $z/W = 0.5$, $Ra = 3.5 \times 10^{12}$. The thick dashed line represents the velocity profiles at h_v

In the experimental results in Fig. 17, the maximum velocity also decreases above h_v however velocity drop can only be observed over a short distance but then the maximum velocity slightly increases to reach $1.05 \times \overline{v}_{max}(h_v)$ at y/H=0.75.

Note that close to the unheated wall a secondary high-velocity region also develops due to the slight heating on this wall. However the main focus will be on the main NCBL flow and the BR flow.

In the vicinity of the heated wall, the heat is mainly transferred from the wall to the NCBL by conduction and convection. The velocity peak in the NCBL is therefore due to the streamwise temperature gradient that generates a local high velocity buoyancy-driven region. In the BR, the flow is mainly driven by entrainment and shear from the high velocity region near the heated wall.

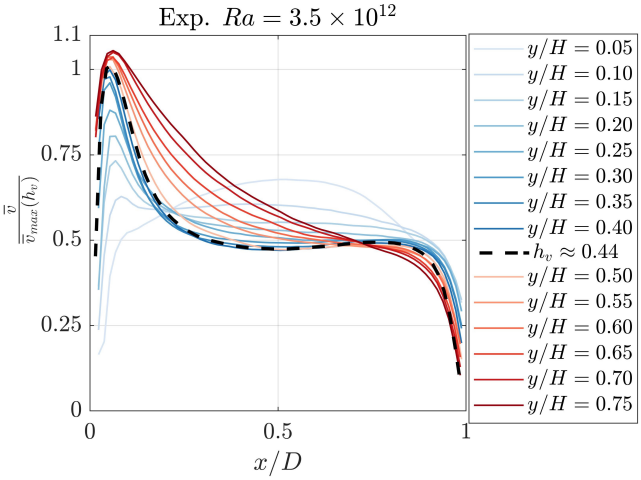

Figure 17: Experimentally obtained velocity profiles at $z/W = 0.5$, $Ra = 3.5 \times 10^{12}$. The thick dashed line represents the velocity profiles at h_v

4.3. Early-turbulence indicator, h_e

Both h_T and h_v proved to be relevant indicators of respectively temperature and velocity based flow changes. However the fact that there are changes in the rate of growth of $\overline{\theta}^*_{min}$, $\Delta\overline{v}$ and $\overline{v}^*_{max}$ prior to h_T and h_v suggests that some transition phenomena may have already started. Thus, in Fig. 18 the streamwise evolution of their y-variation, respectively $(\partial\theta_{min}/\partial y)^*$, and $(\partial v_{max}/\partial y)^*$ are plotted.

From $y/H = 0.3$ to $y/H \simeq 0.45$, $(\partial\theta_{min}/\partial y)^*$ remains relatively constant but then start to deviate before significantly increasing with height.

As for the maximum velocity streamwise variation $(\partial v_{max}/\partial y)^*$, it decreases from $y/H = 0.3$, however its variation is very small until approximately $y/H \simeq 0.45$. From there, $(\partial v_{max}/\partial y)^*$ start to drastically decreases. Because these changes of growth rates are very subtle, it is not possible

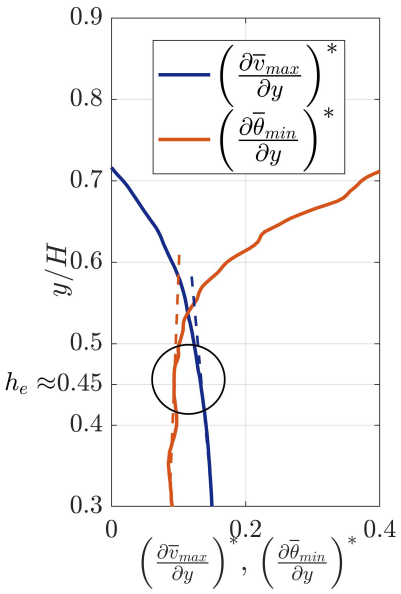

Figure 18: Streamwise evolution of the numerically computed $(\partial\theta_{min}/\partial y)^*$ and $(\partial v_{max}/\partial y)^*$. Thin dashed lines have been plotted to indicate linear trends or significant changes in the quantities growth, an ellipse is used to indicate the location of h_e

to determine their exact location with precision. However, in the present numerical case, the changes in $(\partial\theta_{min}/\partial y)^*$, and $(\partial v_{max}/\partial y)^*$ growth rates occur in very close locations, evaluated here around $h_e \simeq 0.45$. It can be noted that the deviation of $(\partial v_{max}/\partial y)^*$ may occur slightly lower than this of $(\partial\theta_{min}/\partial y)^*$.

Experimentally, due to the noise inherent to PIV measurements, the calculation of $(\partial v_{max}/\partial y)^*$ leads to unusable data. therefore h_e could not be evaluated from it and is evaluated from the growth rate change of $\overline{v}_{max}$ which occurs around $y/H = 0.30 \pm 0.05$ in Fig. 15.

In the present work, only detailed experimental velocities are available within the fluid and therefore $(\partial\theta_{min}/\partial y)$, cannot be evaluated. As a consequence, it is not possible to confirm with the present experimental results if growth rate changes of θ_{min}, and v_{max} occur in the same area. However, as was mentioned in the introduction, the indicator h_e is very similar to the indicator defined and used by Mahajan and Gebhart [22] in an isoflux vertical plate configuration. They observed that the deviation of v_{max} from its laminar trend was a sharp indicator of the beginning of the velocity transition

in a gas. They also mentioned that this changes was *"almost immediately"* followed by a deviation of the temperature across the boundary layer from its laminar trend, which they associated to the thermal transition. Their indicator for v_{max} is the same as the one used in the present paper, whereas this for the temperature is very similar to the changes in $(\partial\theta_{min}/\partial y)^*$ used in the present paper.

Despite natural convection on vertical plate is different from natural convection flow in channel some similar mechanisms are shared and therefore the experimental results of Mahajan and Gebhart [22] support the present numerical observation than changes of $(\partial\theta_{min}/\partial y)^*$, and $(\partial v_{max}/\partial y)^*$ occur in very close locations.

To assess the relevance of h_e to indicate changes in the turbulent quantities, the streamwise evolution of root-mean-square (RMS) quantities of the flow is studied. The RMS of a physical quantity p is defined here as

$$RMS(p) = \sqrt{\overline{p'^2}}. \tag{22}$$

RMS(u), and RMS(θ) are plotted for the numerical case in Fig. 19 and RMS(u) is plotted in the experimental case in Fig. 20.

At $Ra = 3.5 \times 10^{12}$ in Fig. 19 (a), RMS(u) is high in the entrance of the channel, at $y/H = 0.06$, and its maximum is reached in the center of the channel. Then it progressively decreases until h_e. This decrease is plotted in Fig. 19 (a) by the successive blue curves which the color fading from lighter to darker corresponds to growing elevations. From h_e, the maximum of $RMS(u)$ at each elevation is displaced toward the heated wall, and $RMS(u)$ considerably increases. In this case, h_T and h_v, respectively plotted by a thin dashed black and gray line, do not indicate any particular changes. The increase of the fluctuating activity of the wall-normal velocity component confirms the emergence of turbulent transport in the wall normal direction from h_e.

RMS(θ), in Fig. 19 (b), is increasing in the center of the channel, from the inlet to $y/h = 0.86$, height from which it remains approximately the same. At the inlet, the maximum RMS(θ) is reached at the wall and remains there up to approximately y/H=0.13. From there on, and up to h_e, RMS(θ) at the wall remains constant but the maximum RMS(θ) is displaced away from the wall, at $x/D = 0.07$. Then from h_e, RMS(θ) increases at all x-locations but the peak remains around $x/D = 0.07$ up to h_v. Then the maximum RMS(θ) is moved back at the wall. In this case, as can be seen in the magnified view

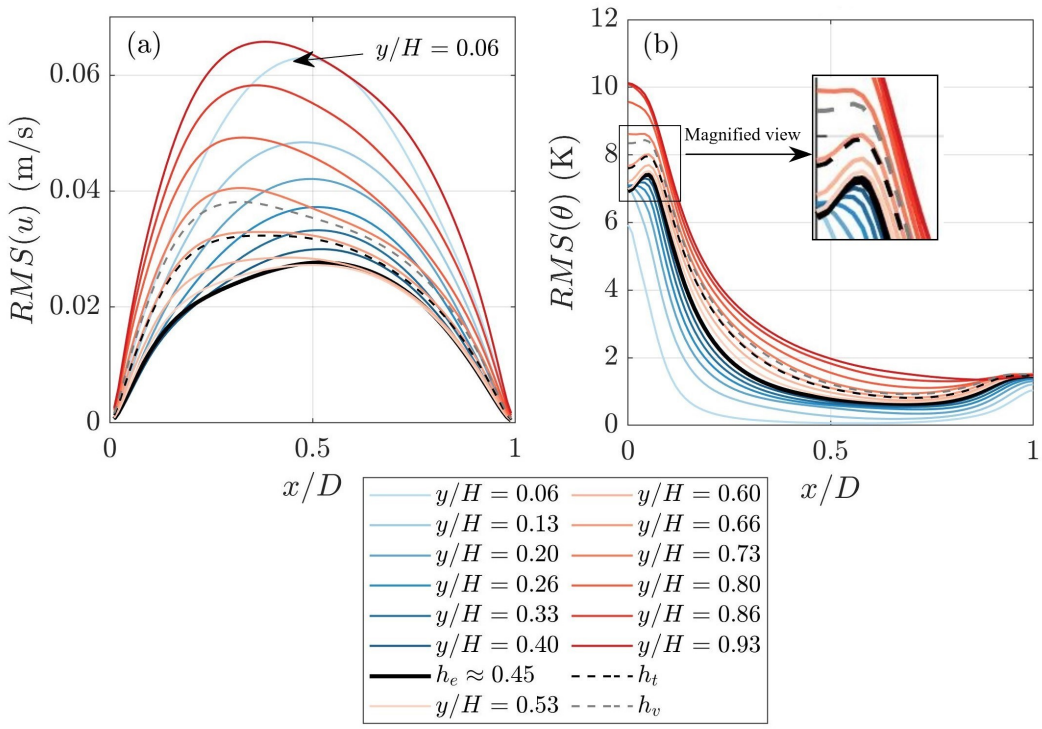

Figure 19: Streamwise evolution of the numerically obtained RMS wall-normal velocity and temperature profiles at $z/W = 0.5$, $Ra = 3.5 \times 10^{12}$, the thick black dashed line plots the RMS at h_e, the thin black dashed line plots the RMS at h_T and the thin gray dashed line plots the RMS at h_v. (a) $RMS(u)$, (b) $RMS(\theta)$

of Fig. 19 (b), h_e indicates the location from which RMS(θ), at the wall, start rising again.

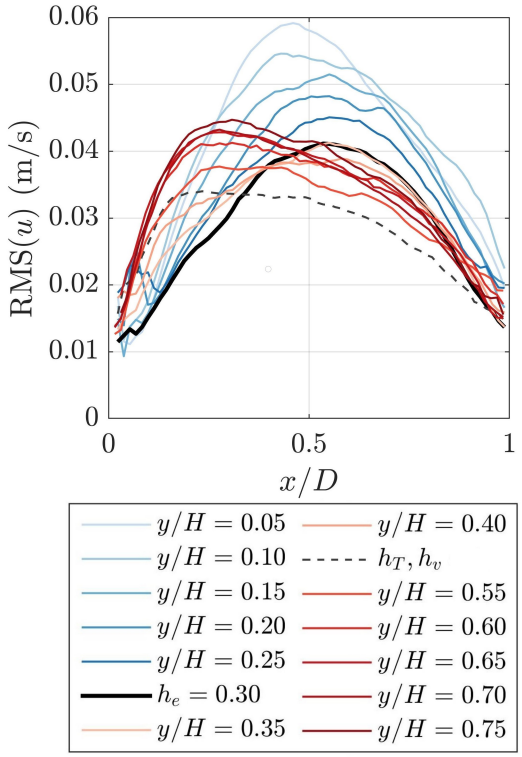

Figure 20: Streamwise evolution of the experimental RMS(u) profiles at $z/W = 0.5$, $Ra = 3.5 \times 10^{12}$, the thick black dashed line plots the RMS at h_e. Only one thin black dashed line plots the RMS at h_T and h_v as now appreciable differences can be observed between the RMS profiles plotted at these two heights.

The experimentally obtained RMS have been plotted in Fig. 20. The RMS quantities variation between the profiles at h_T and h_v were non appreciable so that only one profile have been plotted for these heights.

RMS(u) is plotted in Fig. 20 (a), it clearly appears that h_e indicates a border between two stages. Indeed below h_e, (successive blue color plots) max(RMS(u)) decreases with height and its location is shifted from x/D=0.45 to x/D=0.6. From h_e and above there is a net increase of RMS(u) in the near wall region around $x/D = 0.15$ which indicates that a transition has occurred.

No experimental data from the authors allows to conclude if an increase

of the near wall temperature fluctuations can be observed experimentally at h_e. Nevertheless, note that in the experimental results of Daverat et al. [9] weak turbulent heat transfer, normal to the heated wall were reported near the heated wall, significantly lower than h_v. This is consistent with the numerical observations in which increase in the temperature fluctuating fields can be observed near wall, below h_v.

4.4. Case of $Ra = 1.5 \times 10^{12}$

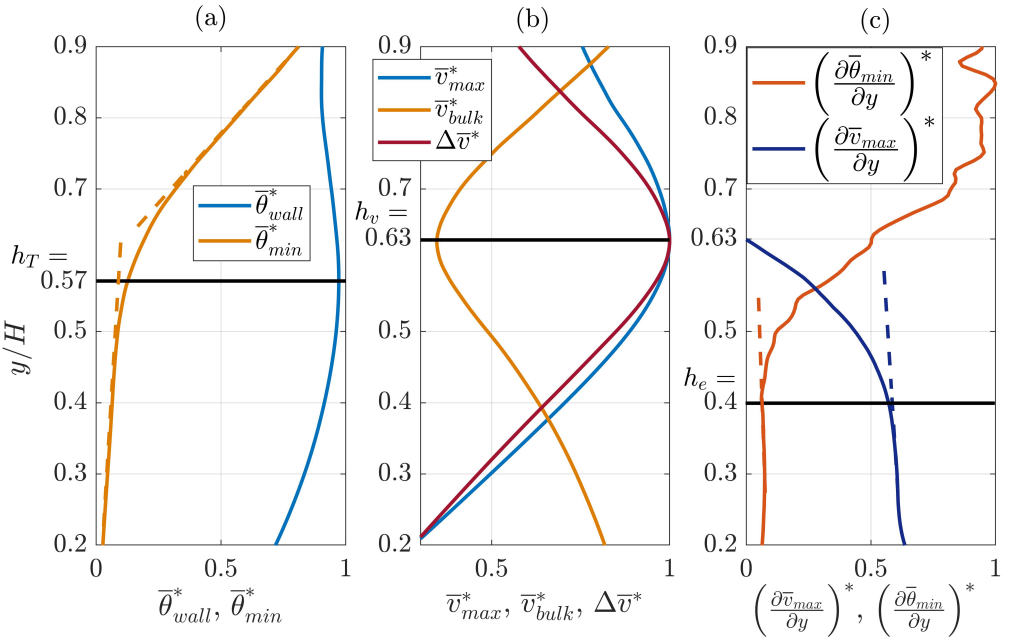

Figure 21: Streamwise evolution of (a) $\overline{\theta}^*_{wall}$ and $\overline{\theta}^*_{min}$, (b) $\overline{v}^*_{max}$, $\overline{v}^*_{bulk}$, $\Delta\overline{v}^*$ (c) $(\partial\theta_{min}/\partial y)^*$ and $(\partial v_{max}/\partial y)^*$. Numerical $Ra = 1.5 \times 10^{12}$, δ_T=1.1 K/m. Thin dashed lines have been plotted to indicate linear trends or significant changes in the quantities growth. h_T, h_v and h_e have been indicated by thick black lines.

The exact same analysis is consistent with the numerical case at $Ra = 1.5 \times 10^{12}$ which indicators have been plotted in Fig. 21. The main differences are that h_T and h_v are located lower at respectively y/H=0.57 and y/H=0.63. h_e is identified around y/H=0.4.

Experimental data of streamwise velocity around h_v and wall temperature have been plotted in Fig. 22. Due to a deviation in the laser sheet parallelism

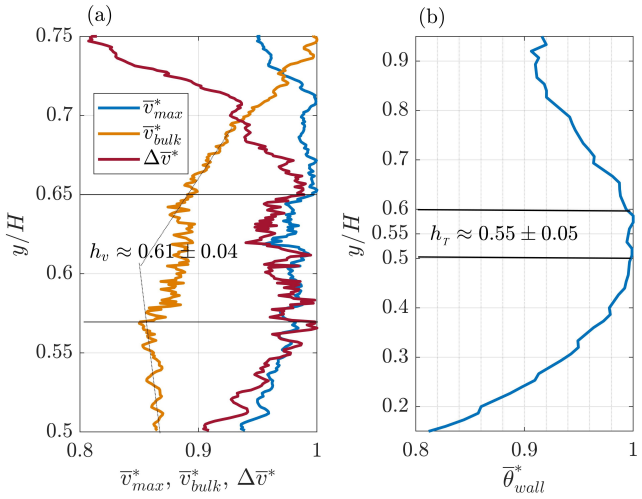

Figure 22: Streamwise evolution of (a) $\overline{v}^*_{max}$, $\overline{v}^*_{bulk}$, $\Delta\overline{v}^*$ and (b) $\overline{\theta}^*_{wall}$ and $\overline{\theta}^*_{min}$ and (c) $(\partial\theta_{min}/\partial y)^*$. Experimental $Ra = 1.5 \times 10^{12}$, δ_T=1.1 K/m. Thin dashed lines have been plotted to indicate linear trends or significant changes in the quantities growth. Thin black lines were plotted to indicate the approximate location of h_v and h_T.

during the PIV measurement in this session, the velocities in the central part of the observed area, between approximately $y/H = 0.57$ and $y/H = 0.65$, are poorly resolved and are therefore poorly reliable. It also appears from the evolution of $\Delta\overline{v}^*$ that h_v is reached in this area. For that reason we evaluated h_v at $y/h \simeq 0.61 \pm 0.04$. Experimentally h_T can be evaluated at $y/H \simeq 0.55$ from the wall temperature, plotted in Fig. 22 (b). In this experimental case it seems clear that h_v is located higher than h_T as it is the case in the numerical results.

It can be observed, that the three indicators defined for the higher Rayleigh number are clearly visible and their relative order is also the same. Moreover regarding h_e in Fig. 21 (b) it seems that the deviation in v_{max} appears also slightly lower than that of θ_{min} which confirms the observation of the numerical results at $Ra = 3.5 \times 10^{12}$ in Fig.18 and is fully consistent with the experimental observations of Mahajan and Gebhart [22].

At $Ra = 1.5 \times 10^{12}$ all the transition indicators in the numerical results have been moved at lower locations in the channel. However, the opposite is observed for the experimental indicators. This could indicate that the strength of the perturbations introduced at the inlet is relatively larger

at the lower Rayleigh number which could result in an earlier transition to turbulence. Since the computational model does not include the whole surroundings of the channel, disturbances need to be introduced at the entrance of the computational domain (section 3.2.2) to obtain results in agreement with experiments. However, the indicators retain the same meaning and are a useful tool to describe transition in natural convection to turbulence.

One can also note the presence of a local minimum of $\overline{\theta}^*_{wall}$ around $y/H = 0.8$ in the numerical results in Fig. 21 (a), which was not present at the higher Rayleigh number. This local minimum can also be observed experimentally at $y/H \simeq 0.9$ for this Rayleigh number in Fig.22. This minimum can also be observed in experimental results from the literature (see e.g. [2]). This local minimum of temperature and the increase of temperature that follows can be expected. Indeed, in the case of an isoflux condition, heat is constantly injected in the channel as the flow travel upwards, and therefore the temperature of the fluid keep increasing in average as the flow travel upwards. The decrease that is observed after h_T is due to the increase of the turbulent heat transfer during the transition process. However, this decrease of temperature at the wall can only be over a certain distance. Indeed, during this decrease, the temperature difference between the wall and the bulk region decreases as well and consequently the turbulent heat transfers between the wall and the bulk region becomes less and less efficient. At what point the wall temperature must increase again to keep dissipating heat from the wall.

4.5. Short discussion and summary

The detailed flow visualization and the indicators defined above allow to propose the following transition scenario, illustrated in Fig. 23. The flow enters like a plug flow but rapidly a high-velocity buoyant region appears and grows near the heated wall because of the conductive and streamwise convective heat transfer from the wall to the NCBL. This accelerating flow region also results in an increase of the shear stresses, both from the wall shear and from the velocity difference in the outer part, between the NCBL and the BR. At one point, the increase of the streamwise velocity in the NCBL is limited by these shears. Consequently the streamwise convective heat transfer is limited as well. However, in order to keep dissipating heat from the wall, other transfer processes must take place. As a result, wall-normal convective heat transfer may start to increase. These transfers, also referred to as turbulent heat transfer, transfer heat and momentum from the wall region into the bulk region and would be the cause of the changes in the

turbulence statistics at h_e. However, at first they are not strong enough to go beyond the onset of stability. Consequently as the flow travels upward the velocity difference keeps increasing and therefore the shear does too, up to h_T and h_v from which a change occurs which tends to locally homogenize the velocity and temperature distributions. However due to the constant heat injection at the wall, after a certain rate of mixing, the wall temperature must increase again as was mentioned at the end of the previous section.

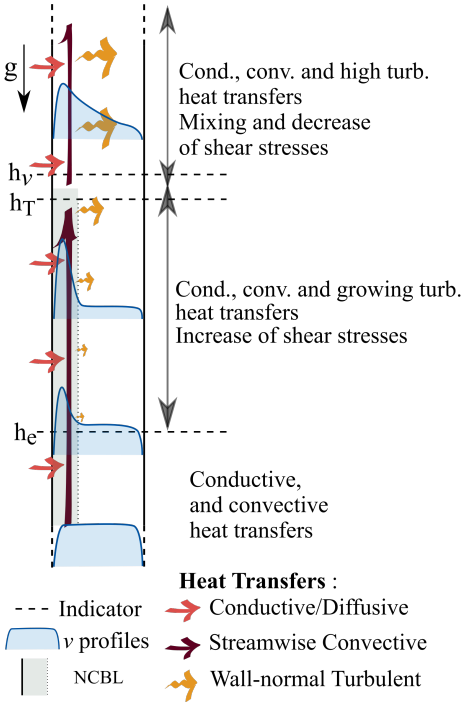

Figure 23: Schematic representation of the transition scenario

Note that this scenario has common elements with the transition scenario of Daverat et al. [9] in an experimental water channel heated on both sides. They attributed the velocity changes to the fact that the velocity boundary layer developing on each wall were joining at some point, therefore limiting the decrease of velocity in the central region of the channel, and consequently limiting also the near wall velocity increase by continuity. They also measured an increase of the turbulent heat transfers lower than h_T and h_v, which reinforce the above proposed scenario, despite Daverat et al. [9] did not explicitly defined a beginning of the transition as was done here with h_e.

All different transition indicators considered in this paper are presented in Table 3. To summarize, h_T was first used by Miyamoto et al. [2] in an asymmetrically heated air channel and has been widely used in the literature since. Its location is varying depending on many parameters related to the Rayleigh number [5], the geometry [2, 3] or the experimental conditions (see e.g. [7, 19, 36, 37]). It indicates the time-averaged temperature changes occurring at the wall and within the flow during the transitional process.

The indicator h_v reproduce the indicator originally defined by Daverat et al. [9] and Li et al. [27] in a symmetrically heated water channel and indicates the changes in the time-averaged streamwise velocity field. It was observed, based on the present numerical and experimental data, as well as data from the literature, that drastic changes in the flow behavior occurred at these heights, which tend to mix and homogenize the flow. Furthermore, given the close spatial proximity between h_T and h_v both these indicators can be considered as indicators of the late stages of transition.

At the same time, h_e can be observed in experimental and numerical results on changes of slopes of the streamwise evolution of $\overline{v}^*_{max}$. These changes happen to be located in a very close location but slightly lower than changes of slope of $\overline{\theta}^*_{min}$ in the numerical results. Despite no detailed experimental temperature measurements were done in the present work, experimental data from the literature suggests that it could also be the case experimentally.

h_e indicates changes in the turbulent quantities which occur at lower heights than h_T and h_v. For this reason, h_e can be considered as an indicator of the early stages of transition. Moreover, this indicator has a similar definition than this which was used to indicate the beginning of the transition in the case of an experimental vertical plate [22]. It therefore be hypothesized that h_e may also indicate the beginning of the transitional process in vertical channel.

Table 3: Summary of the transition indicators considered in this work

Indicator	Height of ...	Stage of transition	Reproduced from
h_T	local max. of $\overline{\theta}_{wall}$	Advanced	air channel - [2]
h_v	max. of $\Delta\overline{v}$	Advanced	water channel - [9][27]
h_e	growth changes of $\overline{v}_{max}$	Early/Beginning	vertical plate - [22]

Finally, the local minimum of the wall temperature, observed in Fig. 21 (a) and Fig. 22 (b), located above h_T and h_v represent an indicator of the late

stages of the transition. In the case of vertical plate flow, the end of transition was reported as the height from which there were no further appreciable changes in the temperature and velocity turbulent intermittencies [22]. In the present case, a longer channel must be studied in order to investigate whether the local minimum of temperature observed here could be associated with the end of transition or if it is only a late indicator of transition. Therefore this indicator was not reported in Table 3.

5. Conclusion

A transitional natural convection channel flow has been studied experimentally and numerically. The case of two heat power 90 W and 230 W, corresponding to Rayleigh numbers of $Ra = 1.5 \times 10^{12}$ and $Ra = 3.5 \times 10^{12}$ were investigated. Experimentally PIV and thermocouples were used for the velocity and temperature measurements, and the external thermal stratification was measured. Numerically, LES methodology with the Vreman SGS model were used to simulate the flow and temperature distributions. In order to mimic the environmental noise inherent to the experimental measurements, inlet velocity disturbances were introduced. To model the experimental ambient temperature stratification, essential to properly model the flow, a stratification of temperature and pressure was applied at the open boundaries of the computational domain.

The experimental and numerical results are used to characterize the transition phenomenon by comparing different indicators of transition that were reproduced from the literature, namely h_T, the maximum temperature at the heated wall, h_v the maximum of the velocity gradient across the boundary layer and h_e, newly defined indicator for vertical channel, which is based on the changes in the variation of the minimum temperature in the bulk region and the changes in the growth rate of the maximum velocity near the heated wall.

Based on both detailed numerical and experimental results, h_v represents a clear border of the velocity transition as from there the width of the hot high velocity buoyant region increases due to the wall-normal momentum transfer inherent to transition. This change is followed by a decrease of the maximum velocity, at least locally in the experimental case. The indicator h_T allows a distinct separation of the evolution of the temperatures in the channel as from this height the temperature inside the channel considerably increases as a consequence of significant increases of the turbulent heat transfer. The

heights h_T and h_v are located very close with h_v being slightly higher than h_T in the numerical results. Given the drastic changes observed in the time-averaged quantities of the flow at these heights, they can be considered as advanced stages of the transition.

Finally h_e is located significantly lower than h_v and h_T and proved to be a relevant indicator to capture changes in the turbulent statistics of the flow and more especially in the wall-normal fluctuating changes, which are characteristic of the turbulent transfers. To that aim this indicator is considered as an indicator of the early stages of turbulence and may even indicates the beginning of transition.

Acknowledgement

The authors would like to thanks Svetlana Tkachenko and Oksana Tkachenko as well as Adrian Vieri for their great help and contribution in setting up the numerical model. The authors thank the financial support provided by the KIC InnoEnergy.

References

References

[1] J. Bloem, Evaluation of a pv-integrated building application in a well-controlled outdoor test environment, Building and Environment 43 (2008) 205–216.

[2] M. Miyamoto, Y. Katoh, J. Kurima, H. Sasaki, Turbulent free convection heat transfer from vertical parallel plates., in: The Eighth International Heat Transfer Conference, volume 4, Hemisphere Publishing Corporation, 1986, pp. 1593–1598.

[3] Z. Chen, P. Bandopadhayay, J. Halldorsson, C. Byrjalsen, P. Heiselberg, Y. Li, An experimental investigation of a solar chimney model with uniform wall heat flux, Building and Environment 38 (2003) 893–906.

[4] T. Yilmaz, A. Gilchrist, Temperature and velocity field characteristics of turbulent natural convection in a vertical parallel-plate channel with asymmetric heating, Heat and Mass Transfer 43 (2007) 707–719.

[5] J. Vareilles, Étude des transferts de chaleur dans un canal vertical différentiellement chauffé : application aux enveloppes photovoltaïques/thermiques, Phd thesis, Université Claude Bernard Lyon 1, 2007.

[6] M. Fossa, C. Ménézo, E. Leonardi, Experimental natural convection on vertical surfaces for building integrated photovoltaic (bipv) applications, Experimental Thermal and Fluid Science 32 (2008) 980–990.

[7] E. Sanvicente, S. Giroux-Julien, C. Ménézo, H. Bouia, Transitional natural convection flow and heat transfer in an open channel, International Journal of Thermal Sciences 63 (2013) 87–104.

[8] C. Daverat, H. Pabiou, C. Ménézo, H. Bouia, S. Xin, Experimental investigation of turbulent natural convection in a vertical water channel with symmetric heating: Flow and heat transfer, Experimental Thermal and Fluid Science 44 (2013) 182–193.

[9] C. Daverat, Y. Li, H. Pabiou, C. Ménézo, S. Xin, Transition to turbulent heat transfer in heated vertical channel - experimental analysis, International Journal of Thermal Sciences 111 (2017) 321–329.

[10] A. G. Fedorov, R. Viskanta, Turbulent natural convection heat transfer in an asymmetrically heated, vertical parallel-plate channel, International Journal of Heat and Mass Transfer 40 (1997) 3849–3860.

[11] G. E. Lau, G. H. Yeoh, V. Timchenko, J. A. Reizes, Large-eddy simulation of turbulent natural convection in vertical parallel-plate channels, Numerical Heat Transfer, Part B: Fundamentals 59 (2011) 259–287.

[12] C. Li, M. Tsubokura, W. Fu, N. Jansson, W. Wang, Compressible direct numerical simulation with a hybrid boundary condition of transitional phenomena in natural convection, International Journal of Heat and Mass Transfer 90 (2015) 654–664.

[13] T. Kogawa, J. Okajima, A. Komiya, S. Armfield, S. Maruyama, Large eddy simulation of turbulent natural convection between symmetrically heated vertical parallel plates for water, International Journal of Heat and Mass Transfer 101 (2016) 870–877.

[14] Y. Zhao, C. Lei, J. C. Patterson, A piv measurement of the natural transition of a natural convection boundary layer, Experiments in Fluids 56 (2015) 9.

[15] Y. Zhao, C. Lei, J. C. Patterson, The k-type and h-type transitions of natural convection boundary layers, Journal of Fluid Mechanics 824 (2017) 352–387.

[16] G. E. Lau, V. Timchenko, C. Ménézo, S. Giroux-Julien, M. Fossa, E. Sanvicente, J. A. Reizes, G. H. Yeoh, Numerical and experimental investigation of unsteady natural convection in a vertical open-ended channel, Computational Thermal Sciences: An International Journal 4 (2012).

[17] O. A. Tkachenko, V. Timchenko, S. Giroux-Julien, C. Ménézo, G. H. Yeoh, J. A. Reizes, E. Sanvicente, M. Fossa, Numerical and experimental investigation of unsteady natural convection in a non-uniformly heated vertical open-ended channel, International Journal of Thermal Sciences 99 (2016) 9–25.

[18] A. G. Abramov, E. M. Smirnov, V. D. Goryachev, Temporal direct numerical simulation of transitional natural-convection boundary layer under conditions of considerable external turbulence effects, Fluid Dynamics Research 46 (2014) 041408.

[19] M. Thebault, Coherent structures and impact of the external thermal stratification in a transitional natural convection vertical channel, Theses, Université de Lyon ; University of New South Wales, 2018. URL: https://tel.archives-ouvertes.fr/tel-02006828.

[20] F. Godaux, B. Gebhart, An experimental study of the transition of natural convection flow adjacent to a vertical surface, International Journal of Heat and Mass Transfer 17 (1974) 93–107.

[21] Y. Jaluria, B. Gebhart, On transition mechanisms in vertical natural convection flow, Journal of Fluid Mechanics 66 (1974) 309–337.

[22] R. Mahajan, B. Gebhart, An experimental determination of transition limits in a vertical natural convection flow adjacent to a surface, Journal of Fluid Mechanics 91 (1979) 131–154.

[23] G. E. Lau, G. H. Yeoh, V. Timchenko, J. A. Reizes, Application of dynamic global-coefficient subgrid-scale models to turbulent natural convection in an enclosed tall cavity, Physics of Fluids 24 (2012) 094105.

[24] G. E. Lau, G. H. Yeoh, V. Timchenko, J. A. Reizes, Large-eddy simulation of natural convection in an asymmetrically-heated vertical parallel-plate channel: Assessment of subgrid-scale models, Computers & Fluids 59 (2012) 101–116.

[25] D. Ramalingom, P. Cocquet, B. A., Numerical study of natural convection in asymmetrically heated channel considering thermal stratification and surface radiation, Numerical Heat Transfer, Part A: Applications 72 (2017) 681–696.

[26] M. Thebault, J. Reizes, S. Giroux-Julien, V. Timchenko, C. Ménézo, Impact of external temperature distribution on the convective mass flow rate in a vertical channel–a theoretical and experimental study, International Journal of Heat and Mass Transfer 121 (2018) 1264–1272.

[27] Y. Li, C. Daverat, H. Pabiou, C. Ménézo, S. Xin, Transition to turbulent heat transfer in heated vertical channel - scaling analysis, International Journal of Thermal Sciences 112 (2017) 199–210.

[28] O. Manca, B. Morrone, V. Naso, A numerical study of natural convection between symmetrically heated vertical parallel plates, in: XII Congresso Nazionale UIT, 1994, pp. 379–390.

[29] E. Sanvicente, Experimental investigation of thermal and fluid dynamical behavior of flows in open-ended channels: Application to Building Integrated Photovoltaic (BiPV) Systems, Phd thesis, INSA de Lyon, 2013.

[30] A. W. Vreman, An eddy-viscosity subgrid-scale model for turbulent shear flow: Algebraic theory and applications, Physics of Fluids 16 (2004) 3670–3681.

[31] G. Lau, Natural convection in building-integrated photovoltaic systems: A computational study, Phd thesis, UNSW-Sydney, 2013.

[32] J. Smagorinsky, General circulation experiments with the primitive equations: I. the basic experiment, Monthly weather review 91 (1963) 99–164.

[33] A. Smirnov, S. Shi, I. Celik, Random flow generation technique for large eddy simulations and particle-dynamics modeling, Journal of Fluids Engineering 123 (2001) 359–371.

[34] G. R. Tabor, M. H. Baba-Ahmadi, Inlet conditions for large eddy simulation: A review, Computers & Fluids 39 (2010) 553–567.

[35] B. Brangeon, P. Joubert, A. Bastide, Influence of the dynamic boundary conditions on natural convection in an asymmetrically heated channel, International Journal of Thermal Sciences 95 (2015) 64–72.

[36] Y. Katoh, M. Miyamoto, J. Kurima, S. Kaneyasu, Turbulent free convection heat transfer from vertical parallel plates : Effect of entrance bell-mouth shape, JSME 34 (1991) 496–501.

[37] Y. Li, H. Pabiou, C. Ménézo, Unsteady heated vertical channel flow in a cavity, International Journal of Thermal Sciences 125 (2018) 293–304.